Making Microlensing Predictions With a New Population Synthesis Galactic Model

Undergraduate Honors Research Thesis

Presented in Partial Fulfillment of the Requirements for Graduation with Honors Research Distinction in Astronomy and Astrophysics in the College of Engineering of The Ohio State University

Macy Huston

Thesis Committee

Dr. Scott Gaudi

Dr. Gregory Lafyatis

Dr. Matthew Penny, Adviser

The Ohio State University
April 10, 2018

Abstract

With the Wide Field Infrared Survey Telescope (WFIRST) in preparation, it is important to have a method of interpreting existing microlensing data and for making predictions for future surveys. Limited by the lack of flexibility and other needed features when using existing models, we created a new, more flexible population synthesis model of the Milky Way. We describe the model's Monte Carlo method for generating catalogs of stars likely to reside in a specific region of the sky and the different Galactic components that come together to achieve this. We compare model output to real data and perform a study of microlensing observables near the Galactic Center. The results highlight areas where disk stars play an important role in microlensing statistics, opposed to the typical assumption in lower latitude surveys that bulge stars dominate, and how disk stars may wipe out the asymmetry of the bulge in microlensing observations.

Acknowledgements

I would first like to thank Dr. Scott Gaudi, whose Introduction to Astronomy course inspired me to get involved in astronomy research, for being my official faculty advisor. I am also grateful for Dr. Paul Martini and all others involved for the Summer Undergraduate Research Program that began my astronomy career. I thank Dr. Gregory Lafyatis for being on my committee and providing advice on presenting my research. Most importantly, I want to thank Dr. Matthew Penny for the endless amounts of help over the past two years.

I want to thank my parents for providing me with the resources I needed to get the education I want and my sister Amber for going three years before me and always answering my questions about how to survive school. Lastly, I thank Esme and Charlie for the endless support in my final year as an undergrad.

Vita

Biographical Information

2010-2014	Circleville High School
2014-Present	The Ohio State University

Fields of Study

Major Field:	Engineering Physics
Minor Field:	Astronomy and Astrophysics

Contents

List of Tables

List of Figures

Chapter 1

Introduction

This work describes a new Galactic model and its use in making microlensing predictions. Before describing the work done, we explain the background behind the study, why the new model is important, and what its goals are.

1.1 Microlensing Events

When a "lens" star passes between a "source" star and an observer, the source's light rays are gravitationally distorted, creating multiple images. Microlensing events occur when this effect is unresolved but shows a time dependent magnification. Planetary companions to the lens star may cause disturbances when they lie near the path of an image. This method's sensitivity to dim stars, small planets, and wide orbits sets it apart from other planet detection methods (direct imaging, transits, and radial velocity). [1]

Magnification due to microlensing is considered significant when the source is within the lens star's Einstein ring,

$$\theta_E = \left(\frac{4GM}{D_{rel} c^2} \right)^{1/2} \tag{1.1}$$

where G is the gravitational constant, M is lens mass and c is speed of light. It is a function of relative distances and lens mass, where D_{rel} is a function of source-observer distance D_s and lens-observer distance D_l,

$$D_{rel} = \left(\frac{1}{D_l} - \frac{1}{D_s} \right)^{-1} \tag{1.2}$$

Note that θ_E is a static property of the system, at least over the timescales considered. The

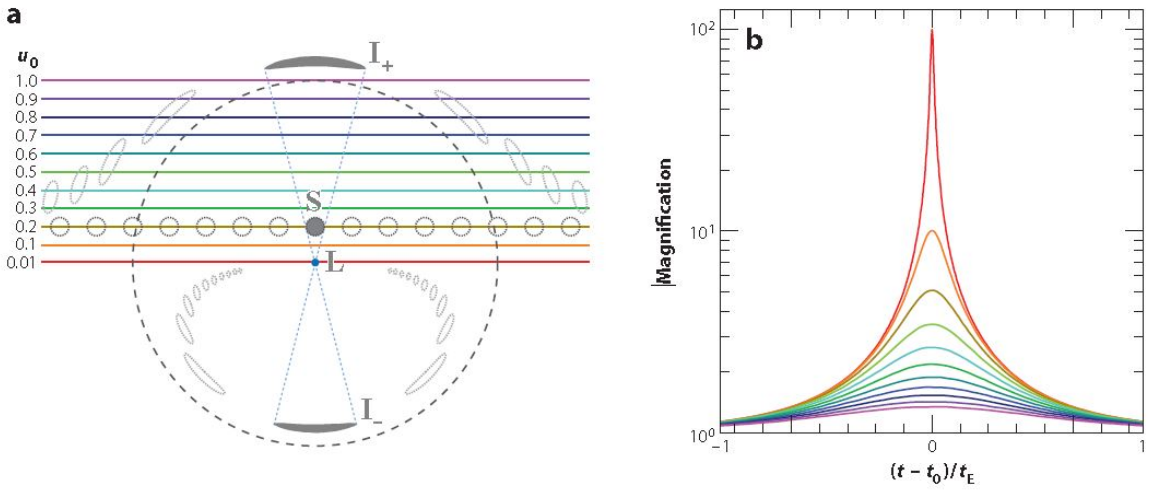

Figure 1.1: Image position and magnification for varying impact parameter (u_0) (a) Impact parameters are normalized to θ_0. The gray distorted circles represent the images produced along the source trajectory for the $u_0 = 0.2$ case. The images vary in size from that of the unlensed source, but surface brightness stays constant; thus, the source is magnified. (b) The magnification occurs over Einstein ring crossing time t_E, peaking at t_0. The height of this peak depends on the impact parameter, and magnification is formally infinite for $u_0 = 0$. Images from Gaudi (2012) [1].

time for the source to cross the Einstein ring radius, the event timescale, is

$$t_E = \frac{\theta_E}{\mu_{rel}} \tag{1.3}$$

Unlike Einstein ring, crossing time is dependent on the kinematics of the system. μ_{rel} is relative proper motion across the sky between the lens and source. Figure 1.1 shows sample light curves for varying angle of closest approach, or impact parameter.

A planetary companion to the lens star can cause a disturbance along these light curves, but this topic is beyond the scope of this study. An in-depth review of planetary microlensing is given by Gaudi (2012) [1].

1.2 Microlensing Surveys

Rather than observing one specific event microlensing event, in this work, we are concerned with the properties of an ensemble of events. Microlensing surveys monitor huge numbers of stars since the events are rare. The three properties we consider in this project are optical depth, timescale, and event rate.

Optical depth is defined as the probability that a star at a specific distance is being microlensed at any moment. As described in Mao (2008) [2], it can be computed as

$$\tau = \int_0^{D_s} n(D_l)\pi\theta_E^2 D_l^2 dD_l, \tag{1.4}$$

where $n(D_l)$ is the number density of lenses at distance D_l. Optical depth is a static concept; it concerns the positions of stars but not their velocities. We are also interested in the dynamical properties. We next consider event rate, how often microlensing events occur for a source star at a specific distance. It is defined by Mao (2008) as

$$\Gamma = \frac{d\tau}{dt} = \int_0^{D_s} n(D_l)\left(\frac{2}{\pi t_E}\right)\pi D_l^2\theta_E^2 dD_l = \int_0^{D_s} n(D_l) 2\mu_{rel}\theta_E D_l^2 dD_l \tag{1.5}$$

These integrals can be computed via Monte Carlo Integration over a catalog of stars drawn from a cone, as described by Awiphan et. al. (2015) [3]. For these calculations, the integrals are converted to sums. We calculate the average optical depth of all the possible source stars in the region as

$$\overline{\tau} = \frac{1}{N_s}\sum^{N_s}\left(\frac{\pi}{\Omega_l}\sum_{D_s>D_l}^{N_l}\theta_E^2\right), \tag{1.6}$$

where Ω_l is the solid angle of the lens region, and N_s and N_l are the number of sources and lenses in their respective regions of sky. For the average time scale, we calculate the average Einstein ring crossing time as

$$\overline{t_E} = \frac{\sum^{N_s}\sum_{D_s>D_l}^{N_l}\theta_E^2}{\sum^{N_s}\sum_{D_s>D_l}^{N_l}\mu\theta_E} = \frac{2\overline{\tau}}{\pi\overline{\Gamma}_{star}}. \tag{1.7}$$

The last property we are interested in is how often microlensing events are expected to occur. Average events per star is computed as

$$\overline{\Gamma}_{star} = \frac{1}{\Omega_l N_s}\sum^{N_s}\sum_{D_s>D_l}^{N_l} 2\mu_{rel}\theta_E. \tag{1.8}$$

One may also consider event rate by area rather than by star. This can be calculated similarly to the previous quantity, as

$$\Gamma_{area} = \frac{1}{\Omega_l\Omega_s}\sum^{N_s}\sum_{D_s>D_l}^{N_l} 2\mu\theta_E = \frac{N_s}{\Omega_s}\overline{\Gamma}_{star}. \tag{1.9}$$

1.3 The Milky Way

Astronomers have long recognized individual structural components of the Galaxy that overlap and fit together to approximate the overall structure. In this view, the Milky Way is a barred spiral galaxy comprised of a dense central bulge, a disk, and a diffuse outer halo. While billions stars have been detected in large Galactic surveys, we only have radial velocity and distances for a relatively small quantity. There is much about the structure of the Milky Way that we do not know, which makes it difficult to model.

The center of the Galaxy is dominated by boxy/peanut shaped bar that we call the bulge, which is densely populated by relatively old stars. The long side of the bar is aligned at some angle from our line of sight toward the GC. The angle of the bar was controversial for some time, but recent studies have converged on a value of $25° - 30°$, for example, Wegg and Gerhard (2013) [4]. When examining Galactic models, one must note that many have yet to adjust to an angle in this range. Evidence exists that the Milky Way's bulge is embedded in a thinner, longer central bar; however, Bland-Hawthorn and Gerhard (2008) [5] explain that this has been exceptionally difficult to characterize, so most models do not contain it as a separate component.

The Galactic disk is comprised of two chemically and kinematically unique components: the thin disk and the thick disk. The thick disk is the older of the two and has no active star formation, while the thin disk has sustained formation. The solar system lies within the Galactic plane, a bit over 8 kpc from the Galactic center. While we have learned a lot in recent years about the solar neighborhood, overall radial and vertical scale heights are not well constrained. Outer disk observations have shown the structure to be complicated. It appears to have an edge, and nearing this edge, it flares and warps away from the Galactic plane. [5]

The Galactic halo contains only about 1% of the total stellar mass; it was likely formed by tidal disruptions of satellite galaxies. While modern studies suggest a more complex, multi-component halo, it is typically modeled as a spheroid of old stars with high random velocities.

This project only concerns the stellar portions of the Galaxy; however, gas and dark

matter contribute significantly to its structure and dynamics. A detailed review of Galactic structure is given by Bland-Hawthorn and Gerhard (2008) [5].

1.4 Project Goals

The complex structure of the Milky Way makes interpretation of microlensing results and predictions of future surveys challenging and uncertain. This issue has become important, as the Wide Field Infrared Survey Telescope's (WFIRST) planetary microlensing survey is currently in planning stages.

In preparation for WFIRST, the United Kindom Infrared Telescope (UKIRT) is performing a microlensing survey on regions near the Galactic Center (GC). An important purpose for this model is to interpret those results and their implications for WIFRST.

Many Galactic models already exist, so the first solution to consider is to take one of them and adapt it to our purposes. We examined existing models, including Besancon [6], TRILEGAL [7], and Galaxia [8], but each lacks key flexibilities and capabilities needed for this project. The Besancon model has an inaccurate Galactic bulge and no flexibility for users. TRILEGAL has some flexibility but does not include kinematics. Galaxia does provide flexibility, but it is very difficult to modify.

The next solution to consider was to use analytic models of the Galaxy, but these cannot account for stellar properties. Thus, necessities for the project, such as magnitude cuts, would be impossible.

With existing models and analytic models eliminated as possible solutions, the remaining task was to construct a new population synthesis model. A population synthesis model performs Monte Carlo simulations over a set of Galactic components to produce a set of stars likely to reside in a conical region leading out from an observer at the sun. Such a model would be able to fulfill all the needs of the project, but this comes at a price. Constructing a new Galactic model code is an extensive project, and generating large catalogs of stars who all have properties to interpolate is computationally expensive. Nevertheless, this project was important for WFIRST planning, so we began construction of the model's outer framework, then worked on improving the components in place. Chapter 2 of this report describes the current form of our Galactic population synthesis model.

Chapter 3 compares this model version's output to real observations. A thorough look at the model includes a test of its capabilities and results in relation to its primary purpose: microlensing predictions. An in-depth examination of microlensing observables across a region surrounding the Galactic center is described in Chapter 4. Model limitations and planned improvements are addressed in Chapter 5. Chapter 6 closes with the implications of the project.

Chapter 2

A New Galactic Model

The project began with a set of two unique goals for a new population synthesis Galactic model. The model should reproduce observed statistical properties of observed populations star by star. The model should have a flexible, modular design to allow easy exploration of parameter variations and the switching out of various components.

2.1 Outer Model Framework

The program created for this project draws catalogs of stars randomly from a set of property distributions (locations, masses, metallicities, etc). The outer framework was set up using the Besancon Model [6] for an initial, testable working form. A population synthesis model consists of multiple sets of stars, with different mass distributions, that come together to produce a galaxy-like set of stars. Each population has its own set of properties and distributions to draw from; the populations in place are the thin disk, thick disk, halo, and bulge.

2.1.1 Field of View

The model returns its results in the form of a catalog of stars visible within the range selected. The model components read in values from a parameter file that the user edits, to specify various properties of the catalog they need. The user chooses a line of sight out from the sun to view, in Galactic longitude and latitude (l, b). They enter a distance out from the sun for the region to extend to. Lastly, they enter a solid angle on the sky over which to observe.

This solid angle is interpreted as a circular region, which results in a conic volume of

space for the model to populate. Each population is generated for this region of space, and they are all output as one catalog.

2.1.2 Basic Stellar Properties

Stars are generated one-by-one and assigned a position, mass, metallicity, velocity, and set of magnitudes. Each population has an equation for stellar mass density across the Galaxy. A random position for the star is selected from within the cone of view, according to the probabilities that this density equation specifies.

Initial mass is drawn from the Initial Mass Function (IMF) given. Metallicity is drawn from an assigned (typically Gaussian) distribution. From these two properties and the given age for the population, a quick magnitude interpolation is performed, as described in the following section, to decide whether the star reaches the cutoff in the proper magnitude band. If it fails, the star is not printed in the catalog, and the program moves on to the next one. If the star passes, it is assigned a velocity, based on a given circular velocity and a velocity dispersion.

2.1.3 Stellar Evolution

The final step in describing a star is to evolve its properties from their initial values to those expected at the star's current age. Its mass must be updated, and its brightnesses in the requested bands must be computed. The model reads in a set of isochrones as its evolutionary basis. These contain lists of stellar properties, on grids of metallicity, initial mass, and age. To get as close as possible to accurate properties for the star in question, 3-dimensional interpolation is performed over these grids. A cubic interpolation method is used when possible, as described by Steffen (1990) [9]. When this method fails, due to non-monotonicity in the data points surrounding the needed value, linear interpolation is used. Lastly, if a star lies outside of the parameter space provided by the grids, it is assigned the properties of the closest track to it; this scenario is rare.

Table 2.1: Stellar mass distributions by population. Local mass densities and normalizations are represented by ρ_0 and d_0. $a^2 = R^2 + \frac{z^2}{\epsilon^2}$, where R is Galactocentric radius, z is height above Galactic plane, and ϵ is axis ratio. ρ_0 and ϵ are listed for each population in Table 2.2

Population	Function	Limits
Thin Disk	$\rho_0/d_0 \times \{\exp(-(a/h_{R+})^2) - \exp(-(a/h_{R-})^2)\}$	age ≤ 0.15 Gyr
	with $h_{R+} = 5000$ pc, $h_{R-} = 3000$ pc	
	$\rho_0/d_0 \times \{\exp(-(0.5^2 + a^2/h_{R+}^2)^{1/2})$	age > 0.15 Gyr
	$-\exp(-(0.5^2 + a^2/h_{R-}^2)^{1/2})\}$	
	with $h_{R+} = 2530$ pc, $h_{R-} = 1320$ pc	
Thick Disk	$\rho_0/d_0 \times \exp(-\frac{R-R_\odot}{h_R}) \times (1 - \frac{1/h_z}{x_l \times (2.+x_l/h_z)} \times z^2)$	$\lvert z\rvert \leq x_l, x_l = 400$ pc
	$\rho_0/d_0 \times \exp(-\frac{R-R_\odot}{h_R}) \times \frac{\exp(x_l/h_z)}{1+x_l/2h_z} \times \exp(-\frac{\lvert z\rvert}{h_z})$	$\lvert z\rvert > x_l$
	with $h_R = 2500$ pc, $h_z = 800$ pc	
Halo	$\rho_0/d_0 \times (\frac{a_c}{R_\odot})^{-2.44}$	$a \leq a_c, a_c = 500$ pc
	$\rho_0/d_0 \times (\frac{a_c}{R_\odot})^{-2.44}$	$a \leq a_c, a_c = 500$ pc
Bulge	$\rho_0 \times K_0(r_s)$	
	where ρ_0 is central density rather than local,	
	K_0 is the modified Bessell function of the	
	second kind, and $r_s = [[(\frac{x}{x_0})^2 + (\frac{y}{y_0})^2]^2 + (\frac{z}{z_0})^4]^{1/4}$	

2.2 Current Model Components

The initial framework was set up using the public version of the Besancon Model [6] for the components, for efficient code debugging, rather than comparison to real data. Following this initial set-up stage, the components of the new model could be incorporated. Besancon Model influence was kept in certain parts, but most major components, including the Galactic bulge stellar distribution, the kinematic system, and the initial mass function, were replaced. The following sections will describe the components currently in place.

2.2.1 Galactic Bulge

The main focus of the present study has been the bulge. The bulge has been replaced with an E3 boxy-shaped bulge, as first proposed by Dwek et. al. (1995) [10], based a more recent set of fits performed by Cao et.al. (2013) [11]. The stellar mass density distribution is included in Table 2.1.

To begin establishing stellar properties, we use the Kroupa (2001) [12] Initial Mass Function. The function is the following 3-component power law, which begins at $M = 0.08 M_\odot$,

Table 2.2: Additional Population Properties

Population Type	Age Gyr	Metallicity 1 [Fe/H](dex)	Metallicity 2 [Fe/H](dex)	ρ_0 $M_\odot/pc^3$	ϵ -
Thin disk	0-0.15	0.01±0.12	-	3.999×10^{-3}	0.0140
	0.15-1	0.03±0.12	-	7.902×10^{-3}	0.0268
	1-2	0.03±0.10	-	6.224×10^{-3}	0.0375
	2-3	0.01±0.11	-	4.020×10^{-3}	0.0551
	3-5	-0.07±0.18	-	5.814×10^{-3}	0.0696
	5-7	-0.14±0.17	-	4.928×10^{-3}	0.0785
	7-10	-0.37±0.20	-	6.590×10^{-3}	0.0791
Thick Disk	11	-0.78±0.30	-	1.34×10^{-3}	-
Halo	14	-1.78±0.50	-	9.32×10^{-6}	0.76
Bulge	10	-0.31±0.31	0.26±0.20	13.26	-
	with weights	0.4	0.6		

for the beginning of H-burning.

$$\xi(M) \propto M^{-a_i}, \tag{2.1}$$

where

$$\begin{aligned} a_0 &= 0.3, \quad 0.01 < M \leq 0.08; \\ a_1 &= 1.3, \quad 0.08 < M \leq 0.50; \\ a_2 &= 2.3, \quad 0.50 < M. \end{aligned} \tag{2.2}$$

Each star must also be assigned a metallicity [Fe/H] and an age. A double Gaussian function, produced by Gonzalez et. al. (2015) [13] describes the metallicity distribution for the bulge, the values for which are given in Table 2.2. The bulge age was set at 10 gigayears, a value fairly consistent among existing models and backed up by observed color-magnitude diagrams.

2.2.2 Disk and Halo

The stellar mass distributions for the thin disk, thick disk and halo were kept from the Besancon model as the model evolved; the equations are shown Table 2.1. We maintain a universal IMF, leaving in place the Kroupa IMF from the bulge. The metallicity and age distributions for these components were adopted from the Besancon Model, as described in Table 2.2.

2.2.3 Stellar Evolution

For stellar evolution, we settled on the MIST isochrone sets- MIST standing for MESA Isochrones and Stellar Tracks [14, 15], and MESA for Modules for Experiments in Stellar Astrophysics [16–18]. The isochrones provide grids of stars, across a set of metallicities, ages, and initial masses. For each point on the grid, the star's current properties are given, from inherent properties like mass and luminosity to observables like magnitudes in specific sets of bands. Through 3-dimensional interpolation, these grids produce the set of properties specific to a generated star.

2.2.4 Kinematic System

Many studies, including the Bulge Radial Velocity Assay [19], suggest cylindrical rotation in the central Galaxy and constant velocity further out. After comparison of real BRAVA data to model output, which will be shown in the following section, a solid body rotation of 45 km/s/kpc was selected for the inner Galaxy. At the radius where this reaches 220 km/s, the model switches to keeping this value as constant for the circular velocity. Velocity dispersions were taken from the Besancon Model.

2.2.5 Extinction

In the current form of the model, no set extinction model is in place. Extinction is quite complicated and difficult to model well. Users are given the opportunity to input their own value for extinction, where it will be treated as constant extinction with a dispersion. The more practical way for the time being for outside users would be to to read in the undimmed data from the model, then apply their own extinction law to it.

For the catalogs used in this paper, extinction values were downloaded from O. A. Gonzales' BEAM Calculator, which follows methods he described in two papers from 2011 to 2012 [20, 21]. A grid of K-band extinctions (A_K) were taken from the range $-5.10^\circ \leq l \leq 10.10^\circ$, $-7.10^\circ \leq b \leq 4.10^\circ$, with spacing 0.05° and box size 3'. For each point on a grid of range $-5^\circ \leq l \leq 10^\circ$, $-7^\circ \leq b \leq 4^\circ$, with spacing 0.25°, the surrounding 5×5 point box on the denser grid was averaged, and standard deviation was calculated. Each point on the latter grid was then assigned its averaged values for A_K and σ_{AK}; these are mapped in Figure 2.1.

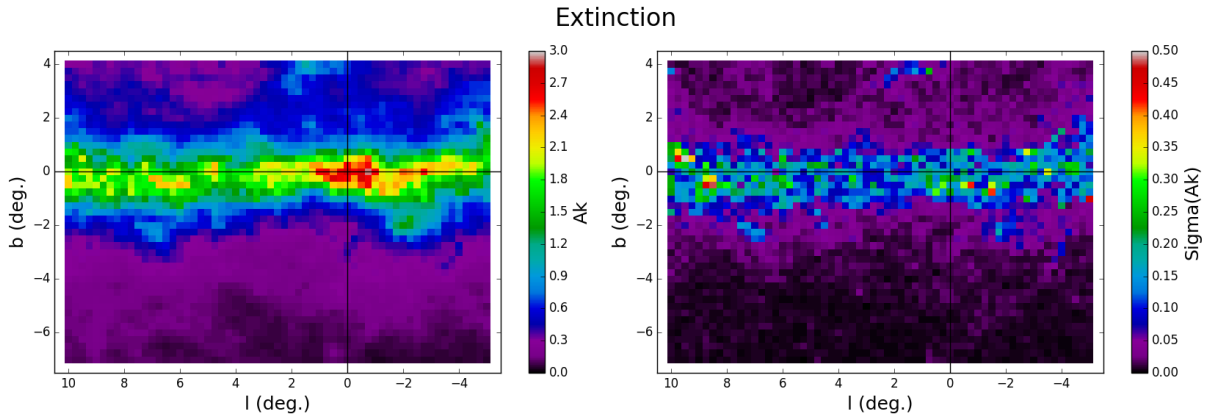

Figure 2.1: Map of A_K and σ_{AK} used for regions surrounding the Galactic center.

The catalogs used in the following sections lie on this grid. Each of the stars in them were assigned a random A_K value from a Gaussian dispersion these maps give. The A_K values were the converted to any other bands that were needed using relationships described by Calamida et. al. (1989) [22]. We calculate these values with the assumption that $R_V = 2.5$, which Nataf et. al. (2013) [23] show is a typical value toward the bulge.

Chapter 3

Model Comparison to Observations

While it is impossible for us to perfectly model the Milky Way stellar population at this time, comparison to observations can help test and constrain model components. Model output was compared to series of real data sets, as described in the following sections.

3.1 Star Counts

In order to test a model's stellar mass distributions, initial mass functions, and evolution, we can compare stellar survey magnitudes to model catalog magnitudes along matching lines of sight. The following subsections describe these comparisons for a set of luminosity functions and color-magnitude diagrams.

3.1.1 Luminosity Functions

To produce a luminosity function, we begin with a collection of stars within a specific region of sky for which we have magnitude values. The stars are sorted and plotted in magnitude bins. Luminosity functions are used to learn about the initial mass function (IMF), particularly low mass stars that have evolved very little over the lifetime of the universe. In terms of Galactic modelling, we use them to check our IMFs, star counts, and stellar evolution.

Two observational luminosity functions are compared to model output in Figure 3.1. First is Holtzman et. al. (1998) [24]. This study uses Hubble Space Telescope (HST) deep photometry of Baade's Window, $(l, b) \simeq (1, -3.9)$, a low-extinction region near the Galactic center. Second is Calamida et. al. (2015) [25]. This study uses data from the Sagittarius Window Eclipsing Extrasolar Planet Search, also performed with HST, in the

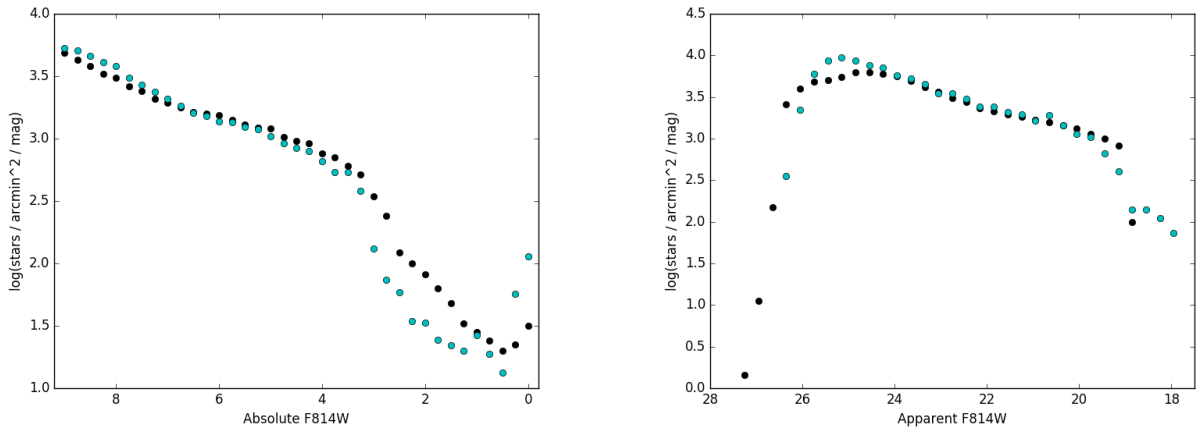

Figure 3.1: Infrared HST luminosity functions. The cited observations are in black, and model data is cyan. (Left) Comparison to Holtzman et.al data. (Right) Comparison to Calamida et. al. data.

region $(l, b) \simeq (1.25, -2.65)$.

Overall, the stellar main sequences match up fairly well. Obvious issues exist at the bright end for the Holtzmann et. al.; this is region is the giant branch, which is more sensitive to stellar properties like age and metallicity. The isochrones used for stellar evolution past the main sequence are likely imperfect, but the scale of errors here will not have a huge impact on microlensing observables.

3.1.2 Color-Magnitude Diagrams

Color-magnitude diagrams plot color (the difference between magnitudes in two bands) against brightness in one band. They require an additional band of data in comparison to luminosity functions but potentially enable diagnosis of errors due to stellar evolution and age distributions.

For observational data, we use the Extended Hipparcos Compilation (XHIP) from Anderson et. al. (2012) [26]. This set of stars comes from the Hipparcos catalog and is extensively cross-referenced with a number of other surveys.The XHIP stars cover regions all across the sky, while the model stars used are all near $b = 0$, $|l| < 10°$. This shows us that the colors and magnitudes of the stars are realistic for an assorted set of Galactic stars.

While relatively sparse, there is a notable region of model stars above the main sequence line. These portion of the CMD is pre-main sequence stars, but this quantity is not expected

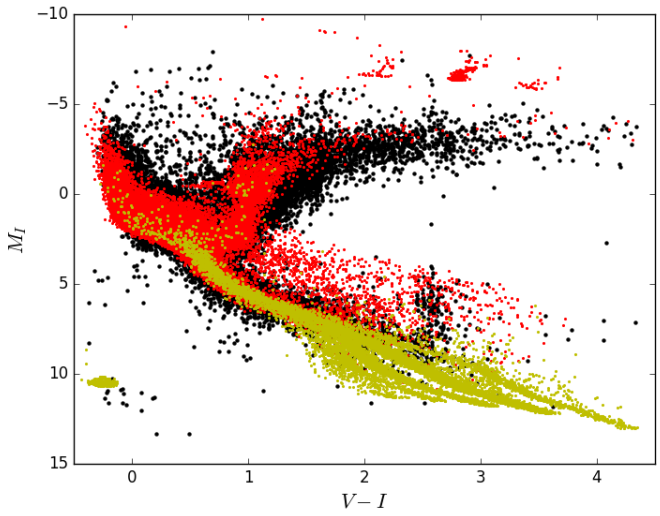

Figure 3.2: Color-magnitude diagram with XHIP data. Model sources (magnitude-cut stars at $K < 18$) shown in red, model lenses (no magnitude cut) in yellow, and XHIP data in black.

based on observation, since the solar neightborhood does not contain many star forming regions. The very red end of the model's giant branch is also notably less populated than expected. The clumps of stars that lie above the giant branch are likely to be those missing from the red giant branch, where their brightnesses were computed to be too high. This problem is likely due to a problem with the isochrone interpolation. If the age grid in this period of evolution is not dense enough, the interpolation process can assign stars values between two stages of evolution to produce values that do not make physical sense.

3.2 Kinematic Observations

In addition to stellar brightnesses, we can observe stellar motions. We use these to test and constrain the kinematic components of the model.

3.2.1 Radial Velocities

Spectroscopy is used to measure stars' velocity along the line of sight. The Bulge Radial Velocity Assay (BRAVA) provided a set of velocities, given by Kunder et. al. (2012) [19], at varying longitude for latitudes of $b = -4°, -6°, -8°$. We compare these to average velocities from the model at a similar range of sight lines in Figure 3.3.

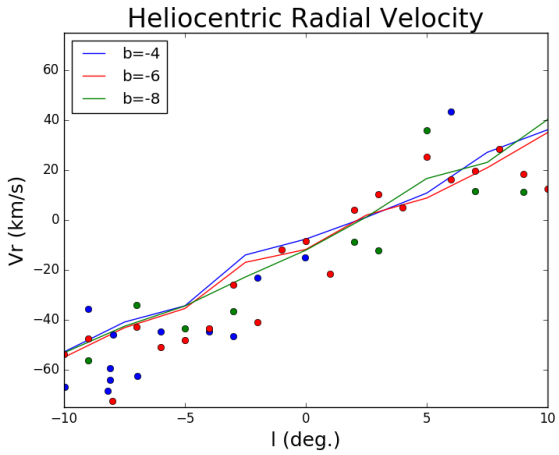

Figure 3.3: Mean heliocentric radial velocities of bulge stars as a function of Galactic longitude, for several latitudes. Model is shown as lines, BRAVA data as points.

The model lines up fairly well with the observations, with possibly slightly low speeds at higher $|l|$. The kinematic model in place was selected because it was a much better fit than the previous one used. In addition to the average values, an important next test of the kinematic system includes velocity dispersions.

3.2.2 Proper Motions

In addition to stellar radial velocity, we can use proper motion across the sky. We look at Hubble data in the $l = 1.25°, b = -2.65°$ sight line analyzed by Clarkson et. al. (2008) [27], compared to our model in Figure 3.4.

First, we compare μ_l between model and data, where $\mu_l = 0$ refers to the average bulge star proper motion. We note that the longitudinal proper motions of model disk stars is closer to zero than observed, while the bulge distribution centers properly. The dispersions of the model are similar to those observed, but the very steep dropoff of disk stars with negative μ_l should be further examined.

Moving on to the μ_b comparison, we note that the modeled bulge stars are a reasonable match to the data. The modeled disk stars, however, are not nearly as dispersed as the observed. Raising the dispersion value of latitudinal disk star motion will be considered for future work.

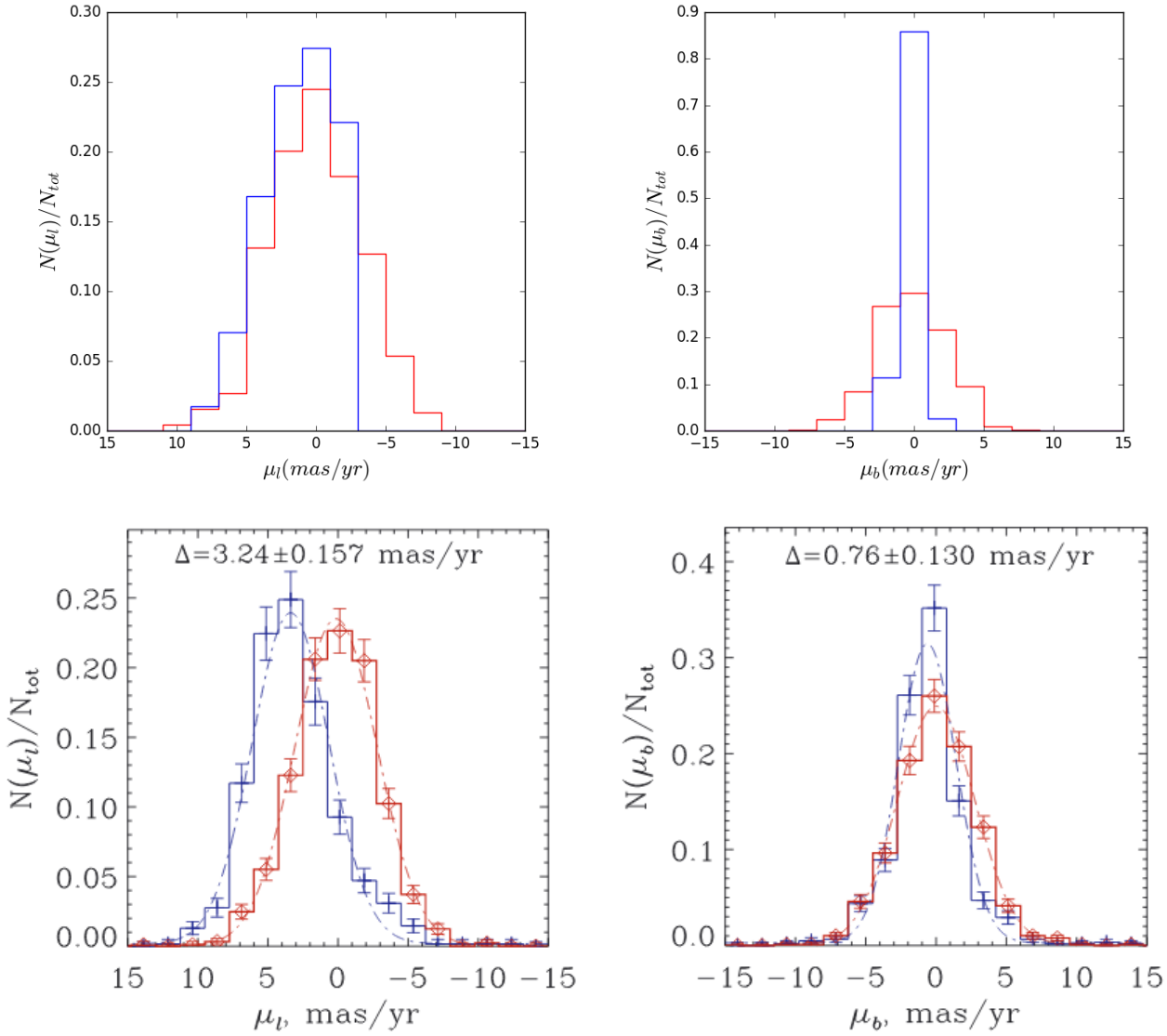

Figure 3.4: Normalized histograms of the proper motions of bulge stars (red) and disk stars (blue). Note that $\mu_l = 0$ is not defined as zero motion across the sky but rather the average longitudinal proper motion for bulge stars. (Top) Model Data. (Bottom) Clarkson et. al. data.

Chapter 4

Predicting Microlensing Observables

The model's designed purpose is predicting microlensing observables, so a thorough description of the model requires a demonstration of this capability. With the current model form described in Chapter 2, a study was performed on a grid of sightlines near the Galactic center. In the following sections, we map microlensing optical depths, average timescales, event rates, and take a closer look at a few specific areas.

4.1 Area of Study

For this sample study, we observe a region of sky near the Galactic center. Catalogs are produced on a grid with spacing 0.25° in the $-5.00° \leq l \leq 10.00°$, $-7.00° \leq b \leq 4.00°$ area, chosen to encompass well-observed areas, as well as the regions of sky observed by the United Kingdom Infrared Telescope (UKIRT) microlensing survey.

In order to calculate the properties below for each of these points, a source catalog and a lens catalog were generated at along each line of sight. Lens catalogs contain all stars within a small area of sky centered on that point, extending outward to a maximum distance of 50 kpc. Source catalogs include all stars above a specific brightness in a larger area of sky centered on that point; in this study $K < 18$ was used. The star counts for the resulting catalogs are shown in Figure 4.1. Note that the lens catalogs have no dependence on brightness and are unaffected by extinction, while the source distributions are heavily impacted by extinction and much less smooth.

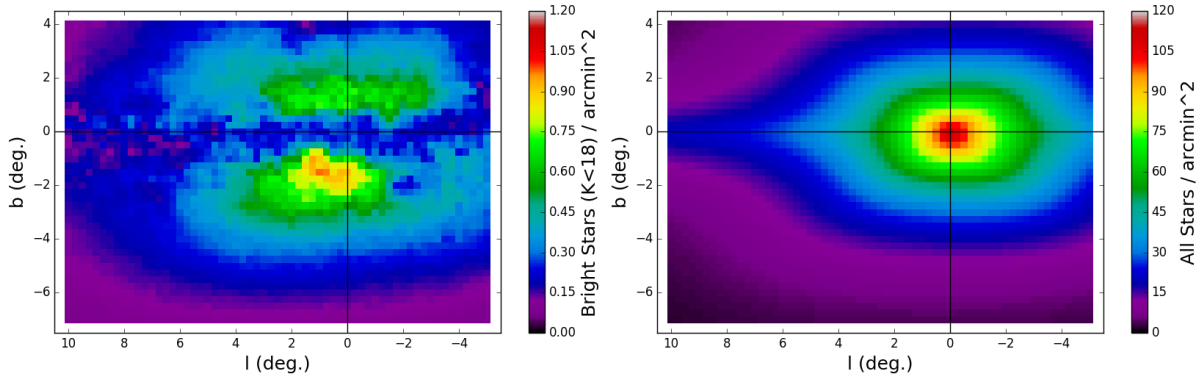

Figure 4.1: Surface density of stars in region of study. (Left) Source ($K < 18$) stars. (Right) All stars.

4.2 Microlensing Observable Maps

For the main portion of the study, we produce maps across the described region of sky that show a set of microlensing observables: optical depth, timescale, and event rate. Refer to the Section 1.3 for definitions and how the calculations are performed (Equations 1.6-9). All of these results are shown in Figure 4.2.

When viewing these plots it is important to keep in mind that $\overline{\tau}$, $\overline{t_E}$, and $\overline{\Gamma}_{star}$ are averaged over all of the possible sources in the region. This helps to erase the effects of extinction and produce smooth maps. This contrasts with Γ_{area}, which depends on the actual number of detectable source stars.

Optical depth is highest toward the Galactic center, as it is the most populated region of the Galaxy. The high optical depth values stretch along the Galactic plane, decreasing much more rapidly as a function of $|b|$ than as a function of $|l|$. It appears to be approximately symmetric both in l and in b.

In contrast, the average timesale is relatively low at the GC. The value at $b = 0$ increases with increasing l, and the latitudinal region of high timescale widens. At $|b| > 5°$, we note that the average timescale increases again for $|l|$ values near 0. A noticeable asymmetry exists, where the short-timescale blobs extend further in positive l than negative l.

Event rate per star has a similar shape to optical depth, compressed in l and stretched in

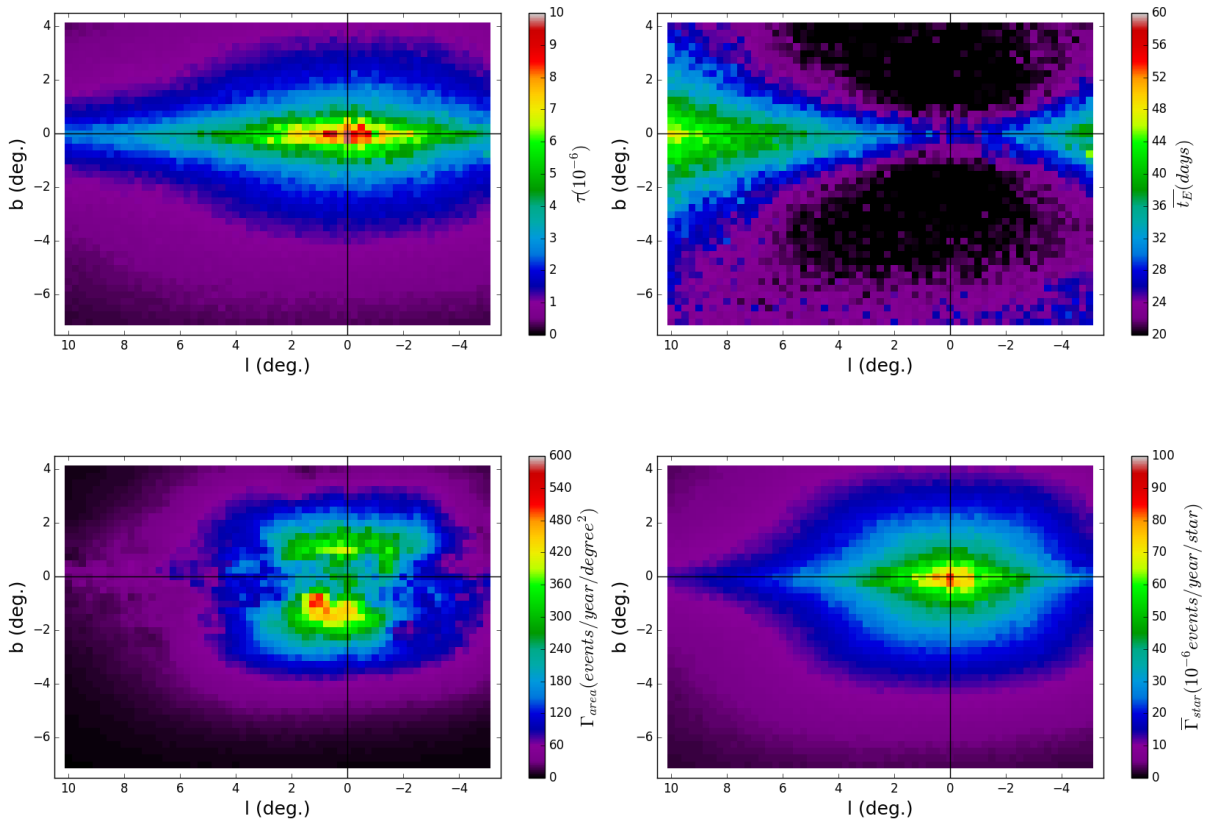

Figure 4.2: Microlensing Observable Predictions. (Top Left) Optical depth. (Top Right) Average Einstein ring crossing time. (Bottom Left) Event rate by area. (Bottom Right) Event rate by star

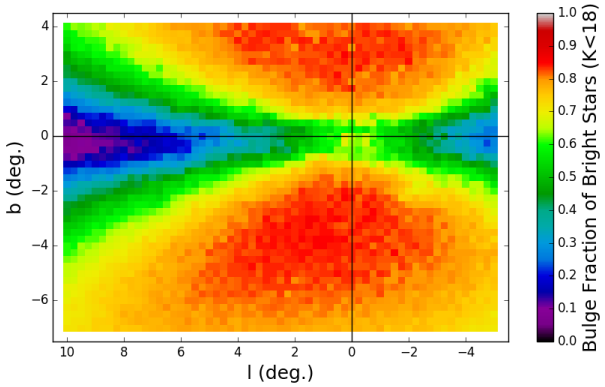

Figure 4.3: Fraction of microlensing source stars that belong to the bulge population. The remaining are disk stars, with some sparse halo stars included.

b. When comparing the maps among one another, we reconsider Equation 1.7, in the form

$$\overline{\Gamma}_{star} = \frac{2\overline{\tau}}{\overline{t}_E}. \tag{4.1}$$

The relationship between the maps helps show how the kinematics of the Galaxy impact event rate, as opposed to simply reflecting the optical depth.

Event rate by area looks like event rate by star with extinction applied. This makes sense when we reverse Equation 1.9 to get

$$\Gamma_{area} = \frac{N_s}{\Omega_s}\overline{\Gamma}_{star}. \tag{4.2}$$

As expected, it is much less smooth than the other three, since extinction plays an important role in the number of source stars.

4.3 Bulge Versus Disk

It is often assumed in microlensing that the stars we observe are in part of the Galactic bulge, but this is not always the case. In the example of the planet UKIRT-2017-BLG-001Lb (Shvarzvald et. al. 2018), a "too red" source star introduces the possibility of a far disk source [28]. This sparked an interest in the relative probability of bulge and disk sources. For this reason, we examine the percentage of microlensing events that stem from bulge stars. First, Figure 4.3 shows the ratio of bulge source stars compared to total.

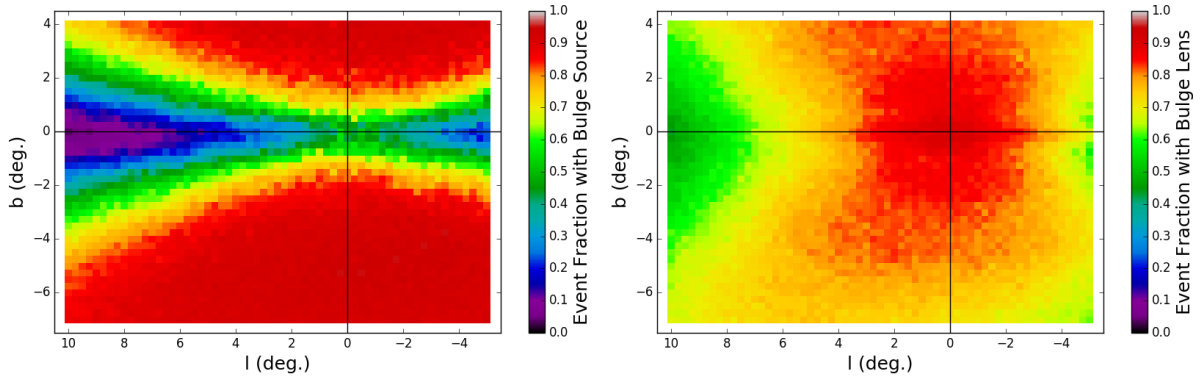

Figure 4.4: Microlensing events involving bulge stars. (Left) Event fraction where the source belongs to the bulge. (Right) Event fraction where the lens belongs to the bulge.

To compare bulge to disk event ratios, we examine 2 scenarios: events with bulge sources and events with bulge lenses. Event rate is calculated for each of these scenarios and is compared to the total event rate calculated previously. These maps are shown in Figure 4.4.

Microlensing studies often assume that the stars involved in their observed events belong to the bulge, but how good is this assumption? When we look at Figure 4.4, there are regions in which stars in the far disk constitute over half of the microlensing sources. This happens along $b = 0$, extending to greater $|b|$ as we move toward greater $|l|$. Most previous microlensing surveys were done at $|b| > 2$, so the bulge source assumption worked for them.

Our lens ratio distribution looks much different. Bulge stars dominate lenses near the GC and fall off in each direction, particularly toward increasing $|l|$ along $b = 0$. It almost looks crescent-shaped, with notably higher source ratios on the positive l side. This asymmetry is discussed further in the following section.

Traditional microlensing fields typically lie below $b = -2$. The bulge source assumption breaks down for $|b| \leq 2$ within $-2 < l < 2$. For the typical microlensing survey in b, then, looking in the $-2 < l < 2$ range is safe for the bulge source assumption. Surveys that cover wider ranges of l or b values very close to the Galactic plane cannot safely make this assumption.

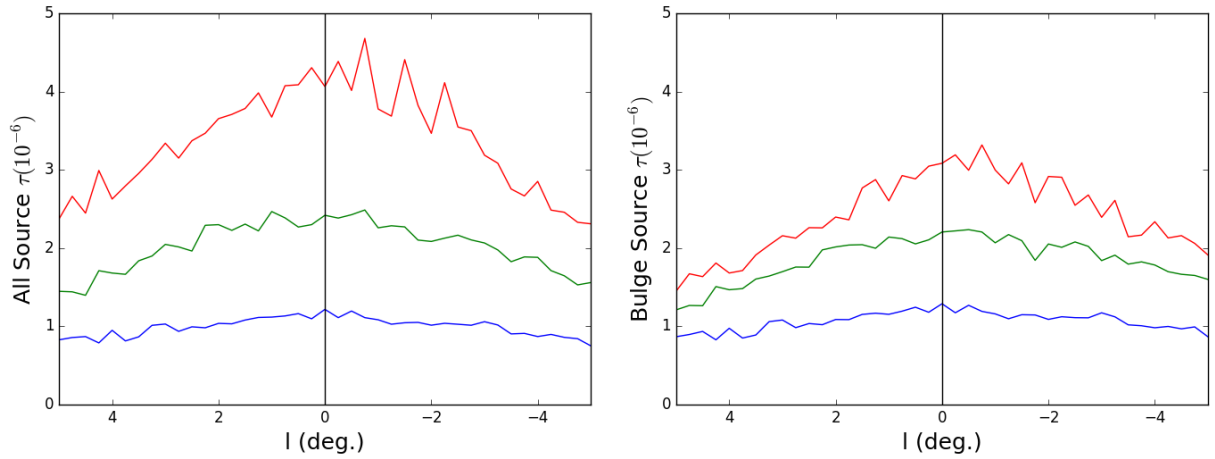

Figure 4.5: Optical depth as a function of l for $b = -1, -2, -4$ (red, green, blue, respectively). (Left) All possible sources. (Right) Bulge sources only.

4.4 Bulge Asymmetry

An interesting effect to look at in these obervables is that of the bar angle. The model's bulge is angled 29.4° away from our line of sight toward the GC, where it is closer to the sun in positive longitudes. This leads us to expect more bright stars at positive longitude (before extinction), since the branch is coser to us. In terms of total number of stars, a similar number of total stars should be on each side of the $l = 0°$ line, but they should be to some extent further dispersed on the positive l side.

The question remains, however, of how this asymmetry affects microlensing. Looking at the maps in Figure 4.2, we only see noticeable asymmetry in timescale. In Figure 4.5, we take a closer look at optical depth values. We also look at the optical depth for bulge-only sources, to see how disk stars can impact the asymmetry.

When looking at the maps in Figure 4.2 and the all source side of Figure 4.5, there is no visible asymmetry, given the error in the Monte Carlo catalog simulations. When we isolate bulge sources, however, the positive l side has non-negligibly lower optical depth values than negative l. This is unsurprising, as the far portion of the bulge will have more disk stars in the foreground than the close portion.

The interesting result is that this effect is not present when both disk and bulge stars are

considered as possible sources. It appears that the close bulge may provide enough possible lenses to far disk sources that asymmetry is insignificant in average optical depth. It would be useful in the future to recompute this graph with larger catalogs to try to decrease error.

Chapter 5

Model Limitations, Errors, and Future Improvements

While a large amount of progress has been made on the model, it remains a work in progress, and there are limitations to its accuracy. With current-day computational and observational errors considered, a perfect model is not achieveable, but we have some specific things that should be noted and must, in the future, be improved.

5.1 Stellar Evolution

During intermediate color-magnitude diagram tests, there was a severe deficit of red giant branch stars. This called for an examination of the isochrones used in stellar evolution. The immediate suspected cause for this issue would be a grid that is so sparse that interpolation could wipe out these stages of evolution. The mass and time grids are quite dense; metallicity, however, is not particularly well covered. In order to avoid skipping important evolutionary phases, it made sense to skip out on intermediate metallicities. Thus, for this implementation of the model, each star was snapped to the metallicity nearest to it for which there was an isochrone.

Improving interpolation across metallicity or obtaining a denser isochrone sampling in metallicity would therefore be valuable. This will be followed by further testing. We will examine luminosity functions from a wider bulge region and attempt to reproduce color-magnitude diagrams from the Optical Gravitational Lensing Experiment (OGLE) and UKIRT.

5.2 Kinematics

The kinematics of the model have not been as extensively tested and modified as we would like to have them eventually. Velocity dispersions from the Besancon model are still in place, while the base velocity values are computed using a solid body rotation and circular motion scheme that greatly contrasts from the Besancon method. Further testing of these dispersions with real data should be performed, and a model that fits better should be incorporated.

5.3 Computational Cost

Computing a population synthesis catalog of stars is a computationally expensive process. Each stellar population must be integrated, and random locations must be determined from the mass density functions. To combat integration time, the model performs an approximation using a series of disks along the sightline to calculate stellar mass rather than using full three-dimensional integration of the complex density functions. Additionally, the complex functions prevent a straightforward random star location selection algorithm. The model instead moves outward along the sightline, populating a small set of these disks at a time, so that the density function does not vary so greatly in the current region. This allows for quicker star placement.

Stellar evolution is also computationally expensive. When performing tests like those above, we need a large set of stars, but only those above a certain brightness. Unfortunately, we cannot know a star's brightness without performing at least some portion of the evolution process. In the current model form, a star takes an average of just under 50 ms to generate. This value has decreased by orders of magnitude since the project first began, but it still adds up when one needs large populations. A large set of source catalogs like those used for the maps in Chapter 4 can take days on a single personal computer.

Chapter 6

Conclusions

The project goal was to create a new Galactic model to help make sense of microlensing observations and to make predictions for future microlensing surveys. We made a new population synthesis model, that uses Monte Carlo simulations to produce a catalog of stars likely to reside in a region of sky chosen by the user. The model is fully functional but will undergo future improvements as more observations are brought in to constrain it. The model represents an important advance in flexibility to users over existing models.

In addition to the model's potential as a tool for future work, the simulated maps of microlensing observables show a few important things. First, infrared surveys close to the Galactic plane will have large numbers of disk stars acting as sources, whereas previous surveys have been performed far enough from the plane that assuming all sources to be in the bulge was safe. We also note that disk sources may wipe out asymmetries in optical depth and event rate that are often searched for in microlensing surveys because of the bulge's angle from our line of sight.

Bibliography

[1] B. S. Gaudi. Microlensing Surveys for Exoplanets. *The Annual Review of Astronomy and Astrophysics*, 50:411–453, 2012.

[2] S. Mao. Introduction to Gravitational Microlensing. *arXiv0811.0441*, 2008.

[3] S. Awiphan, E. Kerins, and A. C. Robin. Besançon Galactic model analysis of MOA-II microlensing: evidence for a mass deficit in the inner bulge. *Monthly Notices of the Royal Astronomical Society*, 456(2):1666–1680, 2016.

[4] C. Wegg and O. Gerhard. Mapping the three-dimensional density of the Galactic bulge with VVV red clump stars. *Monthly Notices of the Royal Astronomical Society*, 435(3):1874–1887, 2013.

[5] J. Bland-Hawthorn and O. Gerhard. The Galaxy in Context: Structural, Kinematic, and Integrated Properties. *The Annual Review of Astronomy and Astrophysics*, 54:529–596, 2016.

[6] A. C. Robin, C. Reyle, S. Derriere, and S. Picaud. A Synthetic View on Structure and Evolution of the Milky Way. *Astronomy and Astrophysics*, 409:523–540, 2003.

[7] L. Girardi, M. Barbieri, M. A. T. Groenewegen, P. Marigo, A. Bressan, H. J. Rocha-Pinto, B. X. Santiago, J. I. B. Camargo, and L. N. da Costa. TRILEGAL, a TRIdimensional modeL of thE GALaxy: Status and Future. *Astrophysics and Space Science Proceedings*, 26:165, 2012.

[8] S. Sharma, J. Bland-Hawthorn, K. V. Johnston, and J. Binney. Galaxia: A Code to Generate A Synthetic Survey of the Milky Way. *The Astrophysical Journal*, 730(1):3, 2011.

[9] M. Steffen. A simple method for monotonic interpolation in one dimension. *Astronomy and Astrophysics*, 239:443–450, 1990.

[10] E. Dwek, R. G. Arendt, M. G. Hauser, T. Kelsall, C. M. Lisse, S. H. Moseley, R. F. Silverberg, T. J. Sodroski, and J. L. Weiland. Morphology, near-infrared luminosity, and mass of the Galactic bulge from COBE DIRBE observations. *The Astrophysical Journal*, 445(2):716–730, 1995.

[11] L. Cao, S. Mao, D. Nataf, N. J. Rattenbury, and A. Gould. A new photometric model of the Galactic bar using red clump giants. *Monthly Notices of the Royal Astronomical Society*, 434(1):595–605, 2013.

[12] P. Kroupa. On the Variation of the Initial Mass Function . *Monthly Notices of the Royal Astronomical Society*, 322(2):231–246, 2001.

[13] O. A. Gonzalez, M. Zoccali, S. Vasquez, V. Hill, M. Rejkuba, E. Valenti, A. Rojas-Arriagada, A. Renzini, C. Babusiaux, D. Minniti, and T. M. Brown. The Giraffe Inner Bulge Survey (GIBS) II. Metallicity distributions and alpha element abundances at fixed Galactic latitude. *Astronomy and Astrophysics*, 584:A46, 2015.

[14] A. Dotter. MESA Isochrones and Stellar Tracks (MIST) 0: Methods for the Construction of Stellar Isochrones. *The Astrophysical Journal Supplement Series*, 222(1):11, 2016.

[15] J. Choi, A. Dotter, C. Conroy, M. Cantiello, B. Paxton, and B. Johnson. MESA Isochrones and Stellar Tracks (MIST) I: Solar-scaled Models. *The Astrophysical Journal*, 823(102):48, 2016.

[16] B. Paxton, L. Bildsten, A. Dotter, F. Herwig, P. Lesaffre, and F. Timmes. Modules for Experiments in Stellar Astrophysics (MESA). *The Astrophysical Journal Supplement*, 192(1):35, 2011.

[17] B. Paxton, M. Cantiello, P. Arras, L. Bildsten, E. F. Brown, A. Dotter, C. Mankovich, M. H. Montgomery, D. Stello, F. X. Timmes, and R. Townsend. Modules for Exper-

iments in Stellar Astrophysics (MESA): Planets, Oscillations, Rotation, and Massive Stars. *The Astrophysical Journal Supplement*, 208(1):42, 2013.

[18] B. Paxton, P. Marchant, J. Schwab, E. B. Bauer, L. Bildsten, M. Cantiello, L. Dessart, R. Farmer, H. Hu, N. Langer, R. H. D. Townsend, D. M. Townsley, and F. X. Timmes. Modules for Experiments in Stellar Astrophysics (MESA): Binaries, Pulsations, and Explosions. *The Astrophysical Journal Supplement*, 220(1):41, 2015.

[19] A. Kunder, A. Koch, R. M. Rich, R. de Propris, C. D. Howard, S. A. Stubbs, C. I. Johnson, J. Shen, Y. Wang, A. C. Robin, J. Kormendy, M. Soto, P. Frinchaboy, D. B. Reitzel, H. Zhao, and L. Origlia. The Bulge Radial Velocity Assay (BRAVA). II. Complete Sample and Data Release. *The Astronomical Journal*, 143:57, 2012.

[20] O. A. Gonzalez, M. Rejkuba, M. Zoccali, E. Valenti, and D. Minniti. Reddening and metallicity maps of the Milky Way bulge from VVV and 2MASS. I. The method and minor axis maps. *Astronomy and Astrophysics*, 534:A3, 2011.

[21] O. A. Gonzalez, M. Rejkuba, M. Zoccali, E. Valenti, D. Minniti, M. Schultheis, R. Tobar, and B. Chen. Reddening and metallicity maps of the Milky Way bulge from VVV and 2MASS. II. The complete high resolution extinction map and implications for Galactic bulge studies. *Astronomy and Astrophysics*, 543:A13, 2012.

[22] J. A. Cardelli, G. C. Clayton, and J. S. Mathis. The relationship between infrared, optical, and ultraviolet extinction. *The Astrophysical Journal*, 345:245–256, 1989.

[23] D. M. Nataf, A. Gould, P. Fouqué, O. A. Gonzalez, J. A. Johnson, J. Skowron, A. Udalski, M. K. Szymański, M. Kubiak, G. Pietrzyński, I. Soszyński, K. Ulaczyk, Ł. Wyrzykowski, and R. Poleski. Reddening and Extinction toward the Galactic Bulge from OGLE-III: The Inner Milky Way's RV 2.5 Extinction Curve. *The Astrophysical Journal*, 769(2):88, 2013.

[24] J. A. Holtzman, A. M. Watson, W. A. Baum, C. J. Grillmair, E. J. Groth, R. M. Light, R. Lynds, and Jr. O'Neil, E. J. The Luminosity Function and Initial Mass Function in the Galactic Bulge. *The Astrophysical Journal*, 115(5):1946–1957, 1998.

[25] A. Calamida, K. C. Sahu, S. Casertano, J. Anderson, S. Cassisi, M. Gennaro, M. Cignoni, T. M. Brown, N. Kains, H. Ferguson, M. Livio, H. E. Bond, R. Buonanno, W. Clarkson, I. Ferraro, A. Pietrinferni, M. Salaris, and J. Valenti. New Insights on the Galactic Bulge Initial Mass Function. *The Astrophysical Journal*, 810(1):8, 2015.

[26] E. Anderson and Ch. Francis. XHIP: An extended hipparcos compilation. *Astronomy Letters*, 38(5):331–346, 2012.

[27] W. Clarkson, K. Sahu, J. Anderson, T. E. Smith, T. M. Brown, R. M. Rich, S. Casertano, H. E. Bond, M. Livio, D. Minniti, N. Panagia, A. Renzini, J. Valenti, and M. Zoccali. Stellar Proper Motions in the Galactic Bulge from Deep Hubble Space Telescope ACS WFC Photometry. *The Astrophysical Journal*, 684(2):1110–1142, 2008.

[28] Y. Shvartzvald, S. Calchi Novati, B. S. Gaudi, G. Bryden, D. M. Nataf, M. T. Penny, C. Beichman, C. B. Henderson, S. Jacklin, E. F. Schlafly, and M. J. Huston. UKIRT-2017-BLG-001Lb: A giant planet detected through the dust. *arXiv1802.06795*, 2018.